Chemical Science

ROYAL SOCIETY OF CHEMISTRY

EDGE ARTICLE

View Article Online
View Journal | View Issue

Cite this: *Chem. Sci.*, 2023, **14**, 9074

All publication charges for this article have been paid for by the Royal Society of Chemistry

Site-selective heat boosting electrochemiluminescence for single cell imaging†

Xiaodan Gou,[a] Yiwen Zhang,[ac] Zejing Xing,[a] Cheng Ma, *[ab] Changjie Mao *[c] and Jun-Jie Zhu *[a]

Received 5th May 2023
Accepted 2nd August 2023

DOI: 10.1039/d3sc02298f

rsc.li/chemical-science

In operando visualization of local electrochemical reactions provides mechanical insights into the dynamic transport of interfacial charge and reactant/product. Electrochemiluminescence is a crossover technique that quantitatively determines Faraday current and mass transport in a straightforward manner. However, the sensitivity is hindered by the low collision efficiency of radicals and side reactions at high voltage. Here, we report a site-selective heat boosting electrochemiluminescence microscopy. By generating a micron-scale heat point *in situ* at the electrode–solution interface, we achieved an enhancement of luminescence intensity up to 63 times, along with an advance of 0.2 V in applied voltage. Experimental results and finite element simulation demonstrate that the fundamental reasons are accelerated reaction rate and thermal convection *via* a photothermal effect. The concentrated electrochemiluminescence not only boosts the contrast of single cells by 20.54 times but also enables the site-selective cell-by-cell analysis of the heterogeneous membrane protein abundance. This electrochemical visualization method has great potential in the highly sensitive and selective analysis of local electron transfer events.

Introduction

In situ/*operando* methods based on electrochemistry have brought deep insights in advancing renewable energy techniques, including new batteries, electrocatalysts, water electrolysis, *etc.*[1] The real-time analysis of interfacial and composition changes under given reaction conditions helped us to exclude some misunderstandings of the mechanism arrived at by bulk analysis. Among various methods, electrochemiluminescence (ECL), a light emission process triggered by electrochemical reactions, stands out because of its unique merits. Thanks to the conversion of electricity to luminescence, ECL has very high sensitivity, a near-zero optical background and fast temporal response to electrical stimulation. The past two decades have witnessed its prosperity in analytical fields of biosensing, environmental detection, medical diagnostics, *etc.*,[2] showing both its extremely high scientific potential and commercial value. With an electron-multiplying charge coupled device (EMCCD) camera and simple lens groups, electrochemiluminescence microscopy (ECLM) not only inherits the advantage of the conventional ECL technique, but is also endowed with high spatial resolution by a simple configuration, becoming the leading technique in *operando* visualization of electrochemical processes.[3–10]

Cell membrane, as a special interface, contains abundant biological information where a panoply of receptors can recognize the external stimuli and initiate the internal responses.[11] There is no doubt that developing the imaging techniques of the cell membrane plays a pivotal role in understanding the mechanisms of many physiological processes including cell–cell communication,[12] activation of signaling pathways,[13] cell migration,[14] disease progression,[15] *etc.* Previous imaging methods mainly resorted to fluorescence, such as total internal reflection fluorescence microscopy (TIRFM),[16,17] confocal laser scanning microscopy (CLSM),[18,19] *etc.* However, the autofluorescence of cells leads to a decrease in the signal-to-noise ratio and the labeling tag is relatively limited. Surface plasmon resonance microscopy (SPRM) does not require a labeling process, but its lateral resolution is restricted by the propagation of evanescent waves.[20,21] Electrochemical techniques such as scanning electrochemical microscopy (SECM) can achieve high spatial resolution but temporal resolution is sacrificed, thus they are not suitable for real-time detection of cell morphology.[22] In the context of the need to ensure both high sensitivity and spatiotemporal resolution, ECL methods have attracted a lot of attention. In comparison to fluorescence microscopy, ECLM is more surface-confined because of the limited lifetime of radical species, and thus it reveals more detailed information

[a]*State Key Laboratory of Analytical Chemistry for Life Science School of Chemistry and Chemical Engineering Nanjing University, Nanjing 210023, P. R. China. E-mail: jjzhu@nju.edu.cn*

[b]*School of Chemistry and Chemical Engineering Yangzhou University, Yangzhou 225002, P. R. China. E-mail: chengma@nju.edu.cn*

[c]*School of Chemistry and Chemical Engineering, Anhui University, Hefei 230601, P. R. China. E-mail: maochangjie@sina.com*

† Electronic supplementary information (ESI) available: Fig. S1–S26 (PDF), Tables S1–S7 (PDF). See DOI: https://doi.org/10.1039/d3sc02298f

about the cell basal membrane.[23,24] In recent years, this technique has been widely used to analyze membrane protein distribution,[25] determine membrane protein contents,[26] image a single biomolecule on cell membranes,[27] observe cell matrix adhesion and cell junctions,[28,29] *etc.*

Nevertheless, one of the fatal problems of this technology is the lack of a strong luminescence system. Although there has been a lot of work devoted to the development of new ECL systems after Leland *et al.*[30] proposed the $Ru(bpy)_3^{2+}$/tri-*n*-propylamine (TPrA) system, the synthesis process is often complex and the luminescence is difficult to be captured by the EMCCD. No work has yet been done to fully exceed the luminescence intensity of the standard $Ru(bpy)_3^{2+}$/TPrA system at suitable concentrations, so this luminescence system is still mainly used in the ECLM field. However, this system has several drawbacks: (i) it needs to reach a voltage above 1 V *vs.* Ag/AgCl to trigger the ECL emission, which may have a great impact on the cell membrane morphology; (ii) it is still a weak light system, having much room for improvement; (iii) it has problems in imaging entities that are relatively far from the electrode because of the surface-confined property.

It is urgent to develop optimization modalities. The factors that influence the final ECL signals in this system include: (i) the kinetics of electrode reactions; (ii) the lifetime of radical cations; (iii) the distribution of reactants. Previous approaches such as shortening the distance between the luminophores and the co-reactants by an intramolecular electron transfer strategy can effectively enhance the luminescence intensity,[31] but are still limited by the modification concentration. Some studies based on the photoelectric effect propose a new type of ECL named the photoinduced electrochemiluminescence (PECL), which can advance the trigger voltage through an applied energy conversion of luminescence to electricity.[32–34] However, this phenomenon is limited to semiconductor electrodes. Here, we boosted the ECL emission of the classic ECL system by inducing local heat through a laser module. Amazingly, the original $Ru(bpy)_3^{2+}$/TPrA system with the strongest luminescence still shows 63-fold increase in ECL intensity. The trigger potential was also advanced by 0.2 V, which is firstly reported *via* photothermal ECLM. And the ECL emission layer around the heating spot became thicker. This method improves the ECL technique through all three factors mentioned above. The local high temperature not only accelerates the ECL reaction rates and advances the overpotential, but also causes thermal convection. Benefiting from the spatial resolution of microscopy, we directly observed the existence of thermal convection and determined its importance in boosting ECL for the first time. Both experimental and finite element simulation show that the thermal convection facilitates the contact between reactants, further promoting the ECL reactions. We also identified that the main influencing species of thermal convection are the co-reactant and its downstream products. Meanwhile, the phenomenon shows site-selective ability and therefore good controllability. With the movement of the laser beam, the enhanced ECL region changes in real time, allowing the imaging or the photothermal treatment of the specified cells. Inspired by all these improved properties, we utilized this heat boosting ECL microscopy (HT-ECLM) to image the suspension cells CEM instead of the commonly used adherent cells which are closer to the electrode surfaces as the imaging objective. Finally, 20.54 times higher contrast images of these suspension cells with short exposure time were achieved. The HT-ECLM strategy proposed in this work broadens the ECLM applications in bioimaging, providing a new opportunity in both cell and material fields.

Results and discussion

Heat boosts the ECL intensity below the trigger potential

Through assembling the laser module in a homemade ECLM, we focused a 730 nm laser on a GCE surface and manipulated the laser intensity. The two added short-pass 700 nm filters and a band-pass 595/645 nm filter (see details in the Instrumentation and General Technologies section) assisted us in excluding the interference between the 730 nm laser and ECL from $Ru(bpy)_3^{2+}$ with the emission peak at 620 nm to the maximum extent. Generally, we employed a three-electrode system containing a GCE as the working electrode, a platinum electrode as the counter electrode and Ag/AgCl as the reference. In the presence of the applied potential from 0 to 1.4 V, the 620 nm ECL emission from 1 mM $Ru(bpy)_3^{2+}$ and 100 mM TPrA will pass through the water-immersion objective ($\times$60, NA = 1.1) and is recorded by the upright EMCCD (Fig. 1A).

When carefully adjusting the laser intensity to 36.18 μW μm^{-2} which cannot be collected by the EMCCD (see details about optimizing the laser intensity in Table S1 and Fig. S1;† the laser intensity was measured after the objective), we found that the place where the laser illuminated showed a brighter spot than other blank spaces and moved in real time with the laser beam, showing great site selective ability. The bright spot also exhibited good stability over 3 h, *i.e.*, it could be collected as long as the ECL reactions were in progress and the laser remained on. The focal plane was on the electrode surface. Concomitantly, the brighter spot appeared at *c.a.* 0.85 V, earlier than the initial voltage (*c.a.* 1.05 V) of the ECL system (Fig. 1B), and the maximum light-emitting voltage is consistent with the blank space, as shown in Fig. 1C and S2†. We define the gain factor as:

$$\text{gain} = \frac{I_{\text{peak}} - I_{\text{background}}}{I_{\text{background}} - I_{\text{offset}}} \quad (1)$$

to describe the ECL enhancement degree in the laser heating region (LHR) quantitatively. Here, I_{peak} stands for the mean ECL intensity obtained using the EMCCD at LHR, $I_{\text{background}}$ represents the average ECL intensity at the blank region without laser heating, and I_{offset} indicates the intrinsic signal acquired with the EMCCD, always around 402.092 (a.u.). As illustrated in Fig. 1D, the maximum of gain reached 63 times at 0.95 V (the ECL gain at different laser intensities is shown in Table S2†). In addition, the value of the gain is much higher at low potential, implying that the laser has a stronger influence at this point, mostly due to the absence of ECL in the blank region. We also noticed that under these experimental conditions where the oxidative-reduction pathway dominated and the catalytic

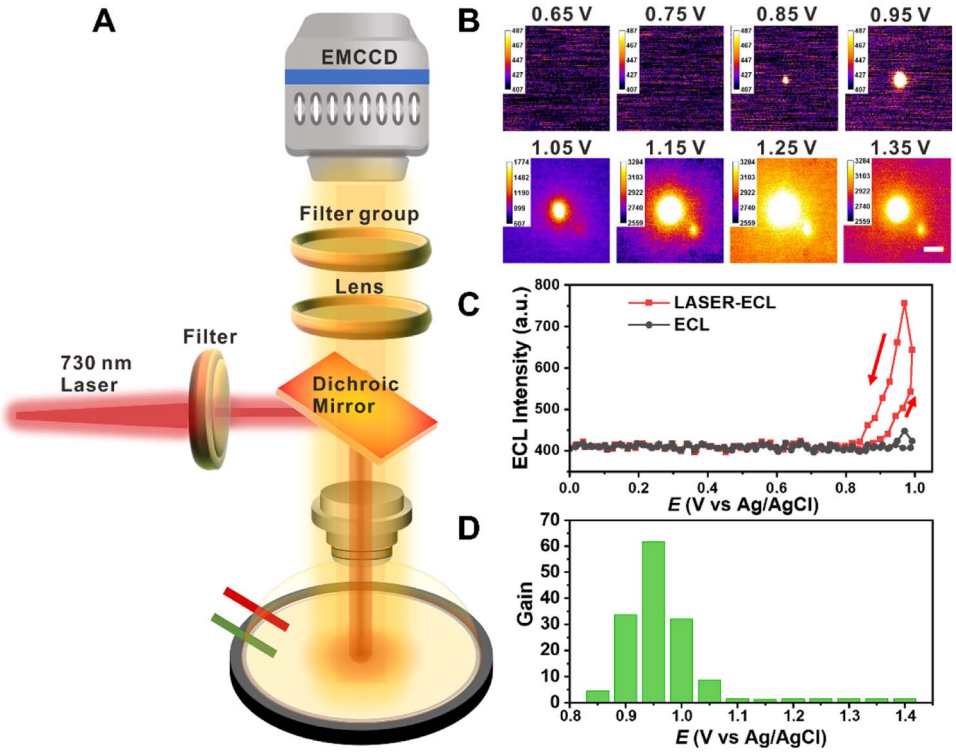

Fig. 1 Observation of heat boosting electrochemiluminescence (HT-ECL). (A) Schematic image of the HT-ECL device. (B) Successive ECL images of the spot heated by laser in 10 mM PBS (pH 7.4) containing 1 mM $Ru(bpy)_3^{2+}$ and 100 mM TPrA with the applied potential from 0 V to 1.4 V at a scan rate of 10 mV s^{-1}. Laser intensity is 36.18 μW μm^{-2}. Scale bar (white) is 10 μm. Exposure time: 200 ms. (C) ECL–potential curves of the place irradiated by laser and the place without laser illumination in 10 mM PBS (pH 7.4) containing 1 mM $Ru(bpy)_3^{2+}$ and 100 mM TPrA. The voltage was cyclically scanned from 0 V to 1.0 V at a scan rate of 10 mV s^{-1}. (D) Diagram of the gain changing with the applied voltage from 0.85 V to 1.4 V. Gain indicates the enhancement of ECL intensity in the laser heating spot compared to other places.

pathway occurred at a higher voltage (*c.a.* 1.3 V), the range of LHR also increased as the voltage was raised. Upon fitting with the Gaussian function, the full width at half maximum (FWHM) of LHR varies with the applied voltage, reaching 3.159 μm at 0.95 V and a maximum of approximately 5.598 μm at 1.15 V (Fig. S3†).

To verify that the HT-ECL was indeed caused by the heating process, we used separate $Ru(bpy)_3^{2+}$, TPrA and PBS solution of the same experimental concentration (*i.e.*, 1 mM for $Ru(bpy)_3^{2+}$, 100 mM for TPrA, 10 mM for PBS) to exclude the possibility that the laser itself changed with the potential. As seen in Fig. S4,† to collect the laser spot, we had to elevate the power density over 331.6 μW μm^{-2} (70 mA), higher than the experimental power density of 36.18 and 49.44 μW μm^{-2} (45 and 55 mA) aforementioned. Nevertheless, we could only observe that the laser bright spot weakened with increasing voltage or stayed unchangeable with change in the voltage (the lower panel in Fig. S4†), probably correlated with the effect of electrode electron loss process on laser intensity[35] and the destruction on the electrode surface. Moreover, the FWHM collected here was 2.524 μm, which was smaller than that in the ECL electrolyte and considered as the size of the laser spot itself. Neither $Ru(bpy)_3^{2+}$ nor TPrA solution undergoes the same phenomenon, revealing that this observation is closely associated with ECL reactions.

Simulation of temperature regulated ECL

For a typical ECL system where $Ru(bpy)_3^{2+}$ acts as the luminophore and TPrA acts as the co-reactant, the ECL pathways are shown in Fig. 2A and Scheme S1.† Simply put, at low potential (around 0.83 V), TPrA is first oxidized into the cation radical $TPrA^{\bullet+}$. This $TPrA^{\bullet+}$ species can firstly generate $TPrA^{\bullet}$ by deprotonation which then reacts with $Ru(bpy)_3^{2+}$ to form $Ru(bpy)_3^{+}$; secondly, it can oxidize $Ru(bpy)_3^{+}$ into an excited state which finally leads to ECL emission. This pathway is named the low oxidation potential (LOP) pathway. Another light-emitting route is the so-called oxidative-reduction route, where $Ru(bpy)_3^{2+}$ is also oxidized into $Ru(bpy)_3^{3+}$ on the GCE surface at a higher potential (start at *c.a.* 1.05 V, maximum at *c.a.* 1.2 V, at room temperature), and subsequently $Ru(bpy)_3^{3+}$ participates in a luminescence emitting reaction with $TPrA^{\bullet}$.

Although there have been several reports about photoinduced ECL before,[36] stating that the advance of potential in the ECL system is due to the holes photogenerated by laser in a semiconductor electrode triggering the ECL reaction, they cannot provide a suitable explanation for our system since the GCE is such a good conductor. Therefore, we made our own speculation that the local enhancement of ECL intensity is due to the localized heating process. To be specific, when a laser beam was added on the GCE surface, the temperature would increase locally to generate a temperature gradient, which

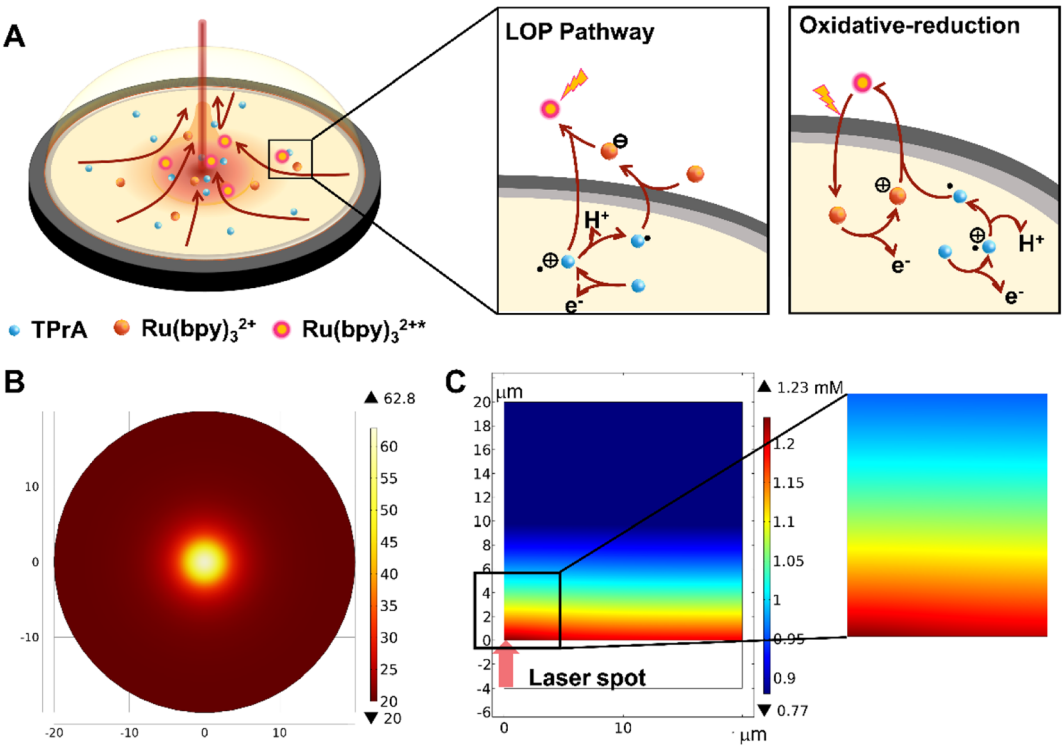

Fig. 2 The mechanism and simulation of HT-ECL. Scheme (A) Illustration of the HT-ECL phenomenon results from thermal convection. The two squares on the right show the two pathways of the ECL reaction. In 1 mM $Ru(bpy)_3^{2+}$ and 100 mM TPrA, both pathways will happen. At potentials lower than around 1.0 V, the LOP route dominates. When the potential is above 1.0 V, the oxidative-reduction route becomes the main pathway to emit light. (B) Temperature distribution on the electrode surface simulated by COMSOL software. (C) Side view image of $Ru(bpy)_3^{2+*}$ simulated by COMSOL software. The red arrow indicates the place where laser irradiates and the laser heating area is locally magnified.

would then induce thermal convection. However, it's difficult to measure the exact temperature change at the LHR due to the minute influence range; we used COMSOL simulation to explore the effect of temperature on the reaction. As seen in Fig. 2B, the temperature in the central region of laser heating reached about 60 °C, while the edge remained at 20 °C. Meanwhile, the simulation result proved that this temperature difference is sufficient to cause thermal convection and enhance the ECL layer (Fig. 2C, and details in the ESI, COMSOL simulation†).

According to the Arrhenius expression $k = Ae^{-E_a/RT}$, where E_a is the activation energy, k is the velocity constant, R is the molar gas constant, T is the reaction temperature, and A is the pre-exponential factor, the reaction rate increases when the temperature rises, which enhances the local ECL, and reduces the overpotential to advance the trigger potential.37 Also, the elevated temperature enhances the diffusion coefficient, which promotes the extension of the ECL layer. The thermal convection drives the aggregation of reactants thereby facilitating the reaction between $TPrA^{\cdot+}$ and luminophores. Thus, it is necessary to compare the contributions of various factors that change during the heating process to the enhancement of the final ECL signal. Firstly, we posit that the stability of radicals remains essentially unchanged or slightly decreases with increase in temperature, as the existing literature indicates a decrease in the luminescence efficiency of the ECL and barely no change in photophysical and photochemical properties with temperature rise.[38,39] Thus, we will primarily compare the impact of convection, diffusion, and electron transfer kinetics on the ECL enhancement. Initially, we generally heated the solution and GCE to 60 °C, where no local temperature gradient was generated. Consequently, the temperature effect only brought about changes in diffusion and electron transfer rates. Upon normalization, an increase of 1.07-fold and 2.26-fold was observed in the current density of $Ru(bpy)_3^{2+}$ and TPrA, respectively. Subsequently, we applied convection using a rotating disk electrode (RDE), with the rotation speed of 1314 rpm corresponding to the convective velocity near the laser spot (for the detailed calculation process refer to eqn S1 and S2†). For $Ru(bpy)_3^{2+}$/TPrA, the observed increases in current density were 2.48-fold and 2.95-fold, respectively (Fig. S5†). Thus, we found that the impact of convection was slightly greater than that of diffusion and electron transfer. Moreover, convection exhibited pronounced effects on both $Ru(bpy)_3^{2+}$ and TPrA, while under the condition of overall heating, the change in $Ru(bpy)_3^{2+}$ was relatively smaller. It is possibly because $Ru(bpy)_3^{2+}$ undergoes an outer-sphere reaction while TPrA undergoes an inner-sphere reaction, making TPrA more susceptible to electrode variations.[40–44] Although both diffusion and electron transfer rates increase with the heating process, we believe that the former has a greater influence on the ECL reaction, as it is predominantly diffusion-controlled.[45] A

comparison between the two was accomplished through COMSOL simulations. When the temperature was set at 60 °C, we independently increased the diffusion coefficient or the electron transfer rates associated with the Butler–Volmer equation (Fig. S10†). According to the simulation results, increasing the diffusion coefficient had a much more significant impact on the luminescent layer than solely increasing the electron transfer rate. In conclusion, we found that in the HT-ECL system, the effect of convection was slightly greater than that of diffusion, and the effect of diffusion was greater than that of the electron transfer rate. Moreover, both simulation (Fig. S11 and S12†) and experimental data indicated that the changes in TPrA were greater than those in $Ru(bpy)_3^{2+}$, suggesting that TPrA may be the primary species influenced by the selective heating process, which will be further discussed in subsequent sections.

Thermal convection promotes the ECL reactions

In corroboration of our opinion, we built a microscopy setup to observe laser-induced thermal convection by fluorescence. (Setup details in Fig. S13A† and Instrumentation section.) The lower dichroic mirror (reflection: 705–900 nm; transmission: 532–690 nm) and 2 short-pass 700 nm filters were used to ensure that 730 nm laser could be focused on the electrode surface and not be recorded by the EMCCD above. The upper dichroic mirror (reflection: 415–470 nm; transmission: 490–720 nm) serves to excite and transmit the fluorescence of $Ru(bpy)_3^{2+}$. 1 mL electrolyte containing $Ru(bpy)_3^{2+}$-doped silica nanoparticles (RuDSN) was put into the electrolytic cell. Subsequently, the laser and light source were turned on and the position change of RuDSN was recorded over a period of time. Although the motion trajectory of RuDSN is not always guaranteed to be in the objective focal plane resulting in a large blurred pattern and some particles might settle on the electrode, stopping the movement because of the influence of gravity, we could still notice that RuDSN started to gather from all directions towards the center heated by laser (a typical particle is marked in Fig. 3A). Furthermore, the average movement of RuDSN within 1 second is 8.23 μm. The longest influence distance exceeded the viewing range, *i.e.*, more than 127.46 μm (from the border to the center of the laser irradiation in Fig. S13E†). Movement of particles hints at the direction of convection (tracking trajectories are marked in Fig. 3B by different colors), proving the virtual existence of thermal convection.

Later, we introduced Nafion into our ECL system. Nafion, a perfluorosulfonated ionomer, can form a polymer electrolyte membrane (PEM) with voids and certain permeability,[46–50] which is often used for entrapping ionic species or immobilizing modified materials. Therefore, after modifying Nafion onto the GCE surface, the diffusion and convection of ECL molecules will be greatly decreased. Given that Nafion could probably reduce the conductivity, a drop of 0.05% Nafion ethanol solution (v/v) was suspension coated on the GCE surface. Although the Nafion may increase the distance between the electrode and the object, the bare areas of the electrode surface could still be discovered and thus helped to maintain the focal plane on the electrode surface. After complete evaporation of the solvent, the bright field image of Nafion on GCE was obtained using the EMCCD. As Fig. S14† shows, the originally smooth surface became rough. Then, we compared the change of ECL on Nafion modified GCE before and after laser was on. Because of poor conductivity, the area covered by Nafion film was shaded black in the ECL field. As expected, the addition of the laser did not cause enhancement of the ECL, most likely due to the poor mobility of the intermediates in the Nafion film and thus the lifetime of intermediates was exhausted (Fig. 3C–E).

Co-reactants are the main species affected by the photothermal effect

As mentioned earlier, we contemplated that TPrA and its electrode products ($TPrA^{\cdot+}$, $TPrA^{\cdot}$) are the species primarily affected during the local heating process. It is mainly proposed for two reasons. First, the ECL layer is mainly dominated by the concentration distribution profile of $TPrA^{\cdot+}$ except in the catalytic pathway; Second, the inner-sphere electrode reactions (TPrA) should be more dependent on the electrode materials than the outer-sphere electrode reactions ($Ru(bpy)_3^{2+}$). In order to compare the difference of electrode reactions of $Ru(bpy)_3^{2+}$ and TPrA, we also performed several experiments as seen in Fig. S15.† That is to say, when a temperature gradient is aroused locally, its influence on the oxidation rate and convection rate of TPrA might be larger than that of $Ru(bpy)_3^{2+}$. To verify this idea, we first altered the concentration of $Ru(bpy)_3^{2+}$ from 50 μM to 10 mM, keeping the concentration of TPrA at 100 mM, to observe the gain of HT-ECL intensity. It is found that when the concentration of $Ru(bpy)_3^{2+}$ is lower than 1 mM, the gain of HT-ECL increased with the increasing concentration. But after reaching 5 mM and 10 mM, this trend disappeared (Fig. 4A). It can be attributed to the different routes of ECL. At low concentrations of $Ru(bpy)_3^{2+}$, the dominant ECL route is the LOP route and oxidative-reduction route, in which $TPrA^{\cdot+}$ decides the ECL layer. When $Ru(bpy)_3^{2+}$ concentration reaches a higher level, the catalytic pathway will occur, where $Ru(bpy)_3^{2+}$ is oxidized to $Ru(bpy)_3^{3+}$ at the electrode, and then $Ru(bpy)_3^{3+}$ oxidizes TPrA into $TPrA^{\cdot+}$ and reacts with $TPrA^{\cdot}$ to generate the excited state. At this situation, $Ru(bpy)_3^{3+}$ will decide the ECL layer. Because TPrA and its downstream species are more influenced, the gain of HT-ECL is much higher at the $Ru(bpy)_3^{2+}$ concentration of 1 mM than at 5 mM and 10 mM. When $Ru(bpy)_3^{2+}$ is at a lower concentration (*i.e.*, 50 μM, 100 μM), the HT-ECL intensity will be limited by very scant luminophores in solution leading to a low value of gain. Thus, increasing the luminophore concentration from 50 μM to 1 mM also augments the HT-ECL intensity, showing the upward trend of gain. We also conducted experiments by keeping the concentration of $Ru(bpy)_3^{2+}$ at 1 mM and varying the concentration of TPrA from 1 mM to 200 mM (Fig. S16†). The results revealed a progressive enhancement in the gain factor with increasing TPrA concentration, eventually

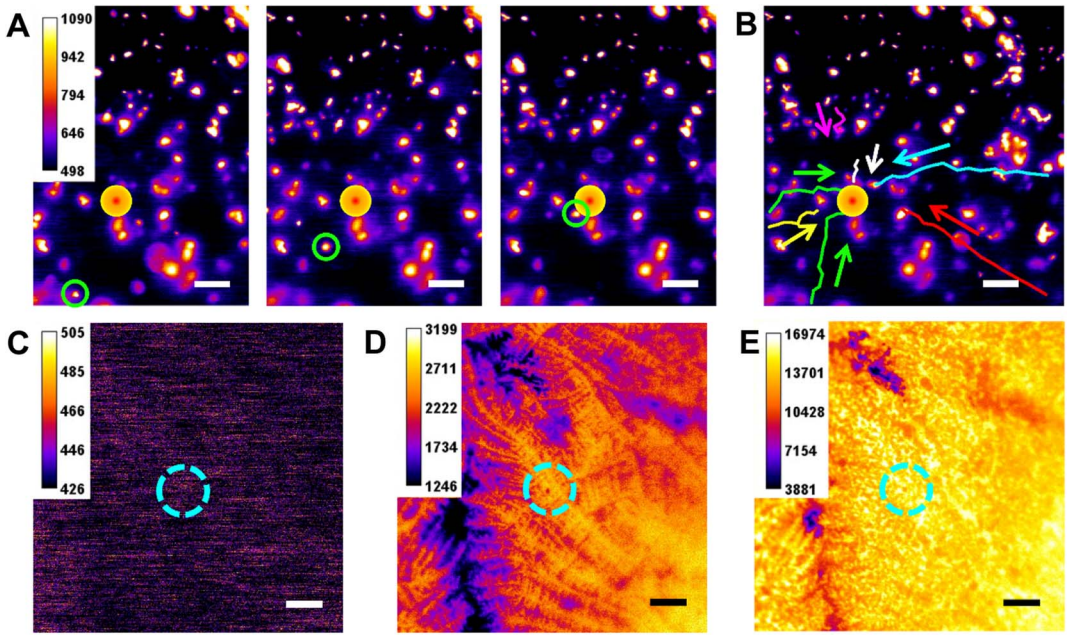

Fig. 3 HT-ECL is promoted by thermal convection and inhibited by the depletion of intermediates. (A) Successive FL images showing the movement of RuDSN in 10 mM PBS (pH 7.4). A typical particle is marked by a green circle, the orange solid circle with red dots in the middle represents the position of the laser. Exposure time: 10 ms. Scale bar (white) is 20 μm. (B) The movement trajectories of seven particles are indicated by lines of different colors, and the arrows show the direction of movements. The trajectory is tracked by imageJ software. Exposure time: 10 ms. Scale bar (white) is 20 μm. (C–E) the HT-ECL images of GCE modified by Nafion in 10 mM PBS (pH 7.4) containing 1 mM $Ru(bpy)_3^{2+}$ and 100 mM TPrA at 0.9 V (C), 1.0 V (D), 1.1 V (E), respectively. The dotted blue circle indicates the laser position where the HT-ECL should have appeared. Exposure time: 200 ms. Scale bar (white for C, black for D and E) is 20 μm.

reaching a maximum value of 42-fold enhancement. The reaction pathway of ECL is mainly determined by the applied voltage and the relative concentrations of $Ru(bpy)_3^{2+}$ and TPrA. In cases where TPrA is relatively dilute, the catalytic pathway predominantly controls the ECL, resulting in a lower enhancement of HT-ECL. As the TPrA concentration continues to increase, the oxidative-reduction and LOP pathways gradually assume dominance, thereby yielding a higher HT-ECL enhancement. Furthermore, as mentioned above, gain is much higher at low potential (*c.a.* 0.95 V) for all concentrations, when $Ru(bpy)_3^{2+}$ has not yet begun to be oxidized by the electrode but it has already reached the onset oxidation potential of TPrA, providing additional evidence.

As known, free-moving molecules are more easily driven by thermal convection than fixed ones. Thus secondly, we changed co-reactants to nitrogen doped carbon dots entrapped by mesoporous silica nanoparticles (NCDs/MSN) through electrostatic attraction. Although NCDs exhibit lower reaction efficiency compared to TPrA, we still observed enhancement phenomena when NCDs were dissolved in a solution containing 1 mM $Ru(bpy)_3^{2+}$ (Fig. S17†). Thus, NCDs/MSN not only contain abundant amine moieties to ensure efficient ECL intensity but have worse mobility. (Characterization details in Fig. S18 and S19†). After dispensing NCDs/MSN on the electrode surface and putting into the solution containing 1 mM $Ru(bpy)_3^{2+}$, it is noticed that the HT-ECL phenomenon was absent in the vicinity of these co-reactant particles under the same experimental conditions, indicating the importance of free-moving co-reactants (Fig. 4B). Then we employed $Ru(bpy)_3(PF_6)_2$ which had poor solubility in aqueous solution to prepare $Ru(bpy)_3^{2+}$ sediment (RuS) on GCE in a solution containing 100 mM TPrA (Fig. S20†). Fig. 4C reveals that the HT-ECL still took place when laser heated the area near the RuS at 1.2 V, but the advance of onset potential disappeared. It can be attributed to the minor dissolution of RuS so that there were still several freely moving luminophores in solution, but the content was too low to trigger the ECL reaction at a lower potential. In comparison, the HT-ECL only emerged when TPrA could move freely, further verifying our aforementioned point of view.

Subsequently, we fixed the luminophores on beads of different sizes to investigate the enhancement effect of HT-ECL when the LOP pathway dominates (corresponding FL images are shown in Fig. S21†). When observing the 1.5 micrometer beads, we found that despite most of the $Ru(bpy)_3^{2+}$ being immobilized on the beads, there was still $Ru(bpy)_3^{2+}$ leaking into the solution, resulting in the HT-ECL phenomenon at the blank electrode. When the HT-ECL region was close to the 1.5 micrometer beads, the ECL gain of the beads increased from 1.53-fold before irradiation to 3.41-fold, and the HT-ECL region appeared to "submerge" the beads (Fig. S22†). This may be because the HT-ECL range in the blank region is larger than the size of the beads. The normalized ECL intensity showed a slight increase in the luminescence range, and the luminescence intensity of neighboring beads also increased, demonstrating the widespread influence range of HT-ECL (Fig. S23†). As for the 5

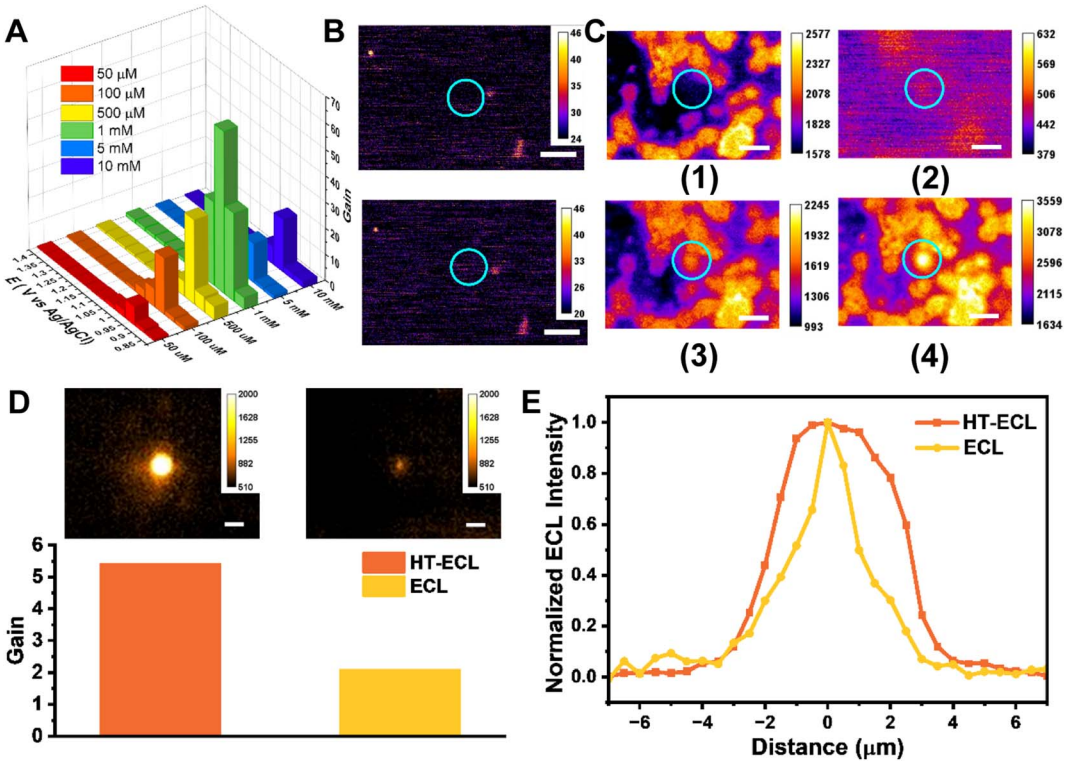

Fig. 4 The main affected species of the heating process are TPrA and downstream species and the enhancement in the LOP pathway. (A) Histogram of gain as a function of applied voltage and emitter concentration. The applied voltage is from 0 V to 1.4 V at the scan rate of 10 mV s^{-1}. The concentration of TPrA remains at 100 mM. (B) The ECL image (upper side) and the HT-ECL image (down side) of NCD/MSNs in 10 mM PBS (pH 7.4) containing 1 mM $Ru(bpy)_3^{2+}$. The blue circle highlights the laser position where HT-ECL should be observed. The comparison between HT-ECL and ECL image indicates no discernible difference between the ECL and HT-ECL image. Exposure time: 500 ms. Scale bar (white) is 20 μm. (C) The ECL and HT-ECL images of RuS in 10 mM PBS (pH 7.4) containing 100 mM TPrA. The image (1) indicates the ECL image of RuS at the potential of 1.2 V, and the other images disclose the HT-ECL images at the applied potential of 1.0 V (2), 1.1 V (3), 1.2 V (4), respectively. The blue circles reveal the place where the HT-ECL will occur. As seen, the place marked by the blue circle in the only ECL image (1) shows no HT-ECL enhancement, while the HT-ECL images (2–4) show obvious HT-ECL enhancement. Exposure time: 200 ms. Scale bar (white) is 20 μm. (D) (Top) The corresponding HT-ECL image (left) and ECL image (right) for the same $Ru(bpy)_3^{2+}$ labeled 5 μm SiO_2 beads in 10 mM PBS (pH 7.4) containing 100 mM TPrA. Applied voltage: 1.3 V. Exposure time: 800 ms. Scale bar: 5 μm. (Bottom) The corresponding HT-ECL and ECL gain for the target bead in the upper image. (E) The normalized ECL intensity along the target bead in (D).

micrometer beads, their size was larger than the HT-ECL range in the blank region, so the "submerging" phenomenon did not occur (Fig. 4D). However, we still observed an increase in luminescence intensity from 2.09-fold before local heat activation to 5.42-fold, accompanied by an expanded luminescence range (Fig. 4E). For the 10 micrometer beads, the luminescence intensity increased from 1.08-fold to 2.61-fold, and there was also a certain degree of expansion in the luminescence range (Fig. S24†). These experiments confirm that in the LOP pathway, the luminescence range indeed increases, and the luminescence intensity experiences a significant enhancement.

Achieving high-contrast ECL images of the single suspension cell by HT-ECLM

All in all, we believe that HT-ECL is a newly discovered phenomenon with higher intensity and a thicker light-emitting layer than pure ECL. We therefore expect to apply this phenomenon in biological imaging to further expand the application of ECLM. Recently, ECLM on single cell studies has been mainly limited to the electrode surface to observe cell membrane proteins,[31] cell adhesion migration,[28] cell basal membranes,[24,51] *etc.*, due to the short lifetime of the intermediate radical. Although there are also papers that extend the ECL layer to image the upper surface of cells using the catalytic pathway,[29,52] the poor specificity and weak signal still restrict its further development. Therefore, we selected suspension cell CEM as a model cell to image, and tried to observe whether HT-ECL could enhance the ECL imaging quality. We first labeled the luminophores on the cell membrane of CEM according to the reported method[23,24] (the detailed labeling process could be found in Materials and methods), and obtained the ECL image as shown in the middle part of Fig. 5B. Although this labeling method achieves positive mode of ECL images, which means that the observation target shows bright ECL emission while the background is black (see the detailed ECL mechanism in Scheme S1†), the signal is always weak. Thus, previous

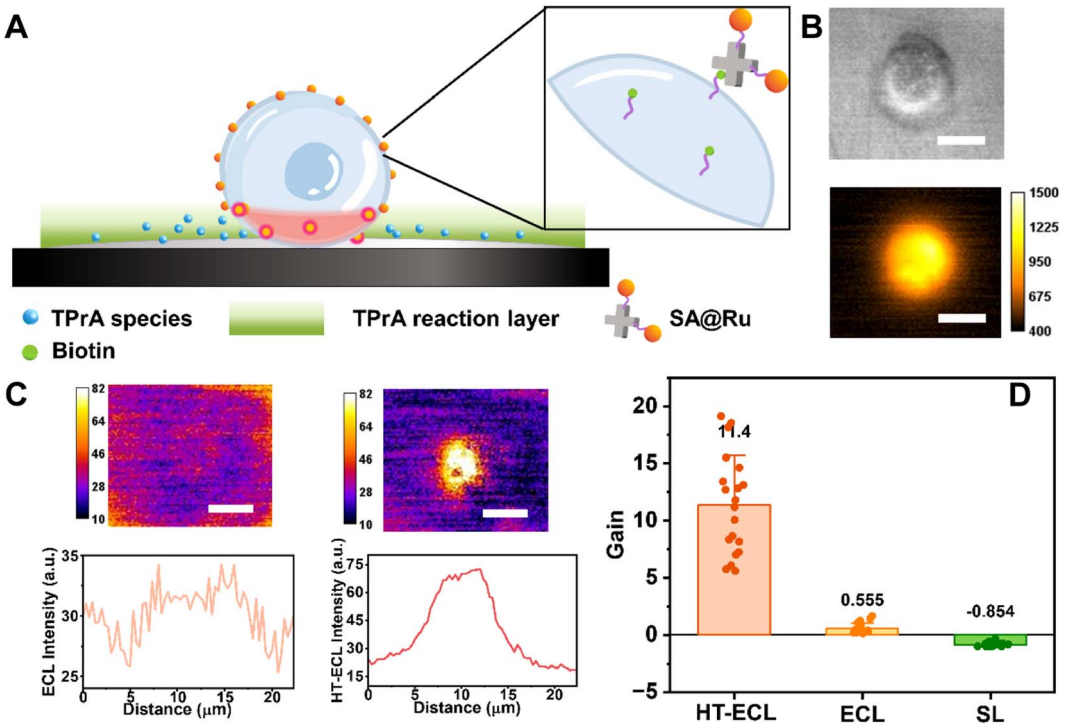

Fig. 5 HT-ECLM obtains high contrast ECL images of CEM at a short exposure time. (A) Schematic illustration of the labeling process on the CEM cell membrane through the specific binding between biotin and streptavidin (SA). (B) The corresponding BF image (top) and FL image (bottom). (C) (Top) processed ECL image (left) and processed HT-ECL image (right) of the same CEM cell. The constant 1.4 V potential was applied in 10 mM PBS (pH 7.4) containing 100 mM TPrA. The detailed image processing procedure could be found in the ESI section.† Scale bar (white) is 10 μm. Exposure time is 1 s. (Bottom) corresponding ECL and HT-ECL intensity along the CEM cell. (D) The statistical gain of HT-ECL ($n = 20$), ECL ($n = 20$) and SL ($n = 20$). The numbers indicate the average values of gain. The error bars suggest the standard deviation.

articles had to elevate the collection parameters (*e.g.*, increasing the exposure time) to get better images.[31,51,53]

Compared to the adherent cells often used in other articles, the suspension cells are located remotely from the electrode surface, so the ECL signal will be further decreased at a low exposure time (*c.a.* 1 s) (middle image in Fig. 5B and the left side of Fig. 5C). Then the laser heated a spot near a CEM cell, and when a voltage of 1.4 V was applied, the luminescence intensity at the cell was significantly enhanced (schematic illustration in Fig. 5A). Note that at this time the signal collected was the sum of the cell HT-ECL and scattering luminescence (SL) of the laser. In order to precisely focus on the HT-ECL, we use the HT-ECL + SL images recorded in the presence of applied voltage to subtract the sole SL images obtained when voltage was off (see Materials and methods for the detailed processing method). As shown in the right image of Fig. 5B and C, the HT-ECL of CEM has indeed been greatly improved in comparison with pure ECL. In addition, for ruling out the possibility that the separate SL intensity changes with the voltage leading to this enhancement occurrence, we performed the same experimental operation and image processing steps on the cells without labeling luminophores. It was found that for the SL signal alone, the intensity decreased with the increase of the charge density, causing a black pattern emerging at the cell region after image processing (Fig. S25†), which is obviously opposite to the phenomenon of HT-ECL. Next, we quantitatively compared the effectiveness of HT-ECL, ECL, and SL on cells with the previously defined gain factor in this paper. It is concluded that for 20 unlabeled cells, the gain values of SL are all negative with the average of −0.854. The gain value of HT-ECL ranges from 5.754 to 19.733, with the median of 11.4 and 20.54 times higher than the gain value of ECL from 0.132 to 1.641 with 0.555 on average (Fig. 5D). It is corroborative that the gain of HT-ECL is much higher than that of ECL, which further proves the superiority of the HT-ECL method.

Furthermore, the HT-ECL method was employed on adherent MCF-7 cells (Fig. S26†), which also exhibits improved imaging contrast. However, the degree of enhancement is 4.38 fold, relatively smaller in comparison with CEM due to their proximity to the electrode surface and inherently higher ECL intensity.

Conclusions

We have discovered the local HT-ECL phenomenon of the model ECL system $Ru(bpy)_3^{2+}$/TPrA by ECLM. The HT-ECL showed a higher ECL intensity (*c.a.* 63 times at 0.95 V), thicker ECL layer and lower trigger potential (*c.a.* 0.85 V) of ECL reactions at the place heated by a laser. By employing RuDSN to directly observe the thermal convection and modifying the Nafion film on the GCE surface to deplete the

lifetime of radicals, along with the COMSOL simulation, we attributed the HT-ECL to the thermal convection and local heat gradient, and the effect sequence is convection > diffusion > electron transfer process. Moreover, experiments with NCDs/MSN immobilizing the co-reactants and RuS immobilizing the luminophores, respectively, have indicated that the main influenced species were TPrA and its downstream electrochemical products due to the different types of electron transfer process between co-reactants and luminophores. This HT-ECLM helped us to greatly improve the image contrast of suspension CEM cells at a relatively low exposure time (1 s). As a newly discovered phenomenon in the imaging domain, we expect that HT-ECL attracts more attention and continues to broaden the application of ECLM. For example, owing to the high site-selectivity of HT-ECLM, a precise PTT and microscopic thermal biology might be achieved. Moreover, because the heating process was induced by a photothermal effect, which has various applications in materials science, we also believe that the HT-ECLM might become a significant tool to evaluate material performances involved in the photothermal conversion process.

Experimental section

Instrumentation and general technologies

Fourier transform infrared spectroscopy (FT-IR) spectra were recorded with a Vector 22 spectrometer (Bruker Corporation, America). The bulk ECL measurements were performed with an MPI-E detection system (Xi'an Remex, China) with a three-electrode system, which consisted of Ag/AgCl (saturated KCl) as the reference electrode, Pt as the counter electrode, and GCE as the working electrode. Electrochemical measurements were performed on a CHI 660D workstation (CH Instruments Inc., Shanghai, China). Scanning electron microscopy (SEM) micrographs were obtained with a Model JSF-7800F scanning electron microscope. High-resolution TEM micrographs were recorded on a JEM 2800 transmission electron microscope. Ultraviolet-visible (UV-vis) absorption spectra were obtained using a UV-3600 spectrophotometer (Shimadzu).

Optical imaging measurements were all carried out on a homemade upright ECL microscopy setup, including microscope configuration and an electrochemical work station. The microscope configuration contained a numerical aperture (NA = 1.10) water-immersion objective (Olympus LUMFLN X60) and an EMCCD camera (Photometrics, Evolve 512 Delta), a filter group, an imaging lens and an additional laser module. When imposing the applied potential on the three-electrode system, ECL emission from $Ru(bpy)_3^{2+}$ passed through a bandpass filter 595/645 nm and were recorded with an EMCCD, which could be triggered by a potentiostat through a TTL signal. The laser module consisted of a laser diode with the center wavelength of 730 nm (HL7302MG, Thorlabs Inc. Shanghai), a current controller (LDC205C, Thorlabs Inc. Shanghai) to drive the laser diode at constant current from 0 mA to 100 mA and a temperature controller (TED200C, Thorlabs Inc. Shanghai) to drive thermoelectric cooler (TEC) elements, respectively. Unless specified, the current used was 45 mA, corresponding to 36.18 μW μm^{-2}, measured with a PM100D Thorlabs optical power meter console with a S121C Thorlabs sensor. The detailed relationship between laser power density and current can be found in Table S1.† When laser was turned on, the laser beam would first pass through a long-pass 725 nm filter to initially purify the laser wavelength into 730 nm, and then a filter group was also added, comprising a long-pass 700 nm filter and a dichroic mirror (reflection band 705/900 nm; transmission band 532/690 nm) and 2 short-pass 700 nm filters along with the bandpass filter 595/645 nm for ECL emission to further eliminate distractions. The corresponding bright field (BF) images and fluorescence (FL) images were obtained using the same microscope device with different filter groups. For BF images, the filter group contained a 400–700 nm reflection mirror. For FL images, the filter group contained a dichroic mirror (reflection band 415/470 nm; transmission band 490/720 nm) to reflect the white light source (LED flashlight), bandpass filter 430/490 nm for excitation, and bandpass filter 595/645 nm for emission, respectively.

Image analysis

The image analysis and processing were performed using Matlab and ImageJ software. To obtain the HT-ECL, ECL, and SL images of the CEM cell, the typical processing method is as follows: first, the initial image sequence of 1 s was recorded with the EMCCD and opened in ImageJ. Second, the voltage data processed using Matlab was in one-to-one correspondence with the image sequence, so as to determine the image sequence with voltage applied and the sequence without voltage applied. Third, 20 original images with 1.4 V applied were superimposed by ImageJ to improve the signal-to-noise ratio followed by subtracting the same superimposed images without voltage applied. For final HT-ECL, ECL, and SL images, the processing methods are exactly the same to acquire rigorous comparative results.

Data availability

The data that support the findings of this study are available from the corresponding author upon reasonable request.

Author contributions

The manuscript was written through contributions of all authors. X. G., Y. Z., and C. M. conceived the study. X. G., Y. Z., and Z. X. performed the experiments. X. G. and Z. X. conducted the COMSOL simulation. C. M. built the microscope setup. X. G., C. M. and J. J. Z. designed the experiments. X. G., Y. Z. and Z. X. analyzed the data. X. G. and C. M. wrote the original draft. J. J. Z., C. M., and C. J. M. advised on the manuscript.

Conflicts of interest

The authors declare no competing financial interest.

Abbreviations

HT-ECL	Heat boosting electrochemiluminescence
ECL	Electrochemiluminescence
LHR	Laser heating region
SL	Scattering luminescence
ECLM	Electrochemiluminescence microscopy
TPrA	Tri-*n*-propylamine

Acknowledgements

This work was supported by the National Natural Science Foundation of China grants 21834004, 22174061 and 21904063; Natural Science Foundation of Jiangsu Province grant BK20190279; Yangzhou University Interdisciplinary Research Foundation for Chemistry Discipline of Targeted Support yzuxk202009; and Foundation of State Key Laboratory of Analytical Chemistry for Life Science grants no. SKLACLS2201; Lvyangjinfeng Talent Program of Yangzhou.

References

1 Y. Yang, Y. Xiong, R. Zeng, X. Y. Lu, M. Krumov, X. Huang, W. X. Xu, H. S. Wang, F. J. DiSalvo, J. D. Brock, D. A. Muller and H. D. Abruna, Operando Methods in Electrocatalysis, *ACS Catal.*, 2021, **11**(3), 1136–1178.

2 W. J. Miao, Electrogenerated chemiluminescence and its biorelated applications, *Chem. Rev.*, 2008, **108**(7), 2506–2553.

3 J. Dong, Y. Xu, Z. Zhang and J. Feng, Operando Imaging of Chemical Activity on Gold Plates with Single-Molecule Electrochemiluminescence Microscopy, *Angew. Chem., Int. Ed.*, 2022, **61**(14), e202200187.

4 A. J. Wilson, K. Marchuk and K. A. Willets, Imaging Electrogenerated Chemiluminescence at Single Gold Nanowire Electrodes, *Nano Lett.*, 2015, **15**(9), 6110–6115.

5 M. M. Chen, W. Zhao, M. J. Zhu, X. L. Li, C. H. Xu, H. Y. Chen and J. J. Xu, Spatiotemporal imaging of electrocatalytic activity on single 2D gold nanoplates *via* electrogenerated chemiluminescence microscopy, *Chem. Sci.*, 2019, **10**(15), 4141–4147.

6 S. Pan, J. Liu and C. M. Hill, Observation of Local Redox Events at Individual Au Nanoparticles Using Electrogenerated Chemiluminescence Microscopy, *J. Phys. Chem. C*, 2015, **119**(48), 27095–27103.

7 M. J. Zhu, J. B. Pan, Z. Q. Wu, X. Y. Gao, W. Zhao, X. H. Xia, J. J. Xu and H. Y. Chen, Electrogenerated Chemiluminescence Imaging of Electrocatalysis at a Single Au-Pt Janus Nanoparticle, *Angew. Chem., Int. Ed. Engl.*, 2018, **57**(15), 4010–4014.

8 H. Zhu, D. Jiang and J.-J. Zhu, High-resolution imaging of catalytic activity of a single graphene sheet using electrochemiluminescence microscopy, *Chem. Sci.*, 2021, **12**(13), 4794–4799.

9 H. Zhu, R. Jin, Y. C. Chang, J. J. Zhu, D. Jiang, Y. Lin and W. Zhu, Understanding the Synergistic Oxidation in Dichalcogenides through Electrochemiluminescence Blinking at Millisecond Resolution, *Adv. Mater.*, 2021, **33**(48), e2105039.

10 H. Zhu, R. Jin, D. Jiang and J. J. Zhu, Perturbation Electrochemiluminescence Imaging to Observe the Fluctuation of Charge-Transfer Resistance in Individual Graphene Microsheets with Redox-Induced Defects, *ACS Appl. Mater. Interfaces*, 2019, **11**(50), 46666–46670.

11 R. Ranganathan, Signaling across the cell membrane, *Science*, 2007, **318**(5854), 1253–1254.

12 K. Y. Xun, K. Pei, X. J. Liu, X. Y. Peng, Y. L. Du, L. P. Qiu and W. H. Tan, Cell-Membrane-Anchored DNA Nanoplatform for Programming Cellular Interactions, *J. Am. Chem. Soc.*, 2019, **141**(45), 18013–18020.

13 J. Massague, TGFbeta signalling in context, *Nat. Rev. Mol. Cell Biol.*, 2012, **13**(10), 616–630.

14 G. Nardone, J. O. D. La Cruz, J. Vrbsky, C. Martini, J. Pribyl, P. Skladal, M. Pesl, G. Caluori, S. Pagliari, F. Martino, Z. Maceckova, M. Hajduch, A. Sanz-Garcia, N. M. Pugno, G. B. Stokin and G. Forte, YAP regulates cell mechanics by controlling focal adhesion assembly, *Nat. Commun.*, 2017, **8**, 15321.

15 M. Yang and W. J. Brackenbury, Membrane potential and cancer progression, *Front. Physiol.*, 2013, **4**, 185.

16 M. C. Dos Santos, C. Vezy and R. Jaffiol, Nanoscale characterization of vesicle adhesion by normalized total internal reflection fluorescence microscopy, *Biochim. Biophys. Acta, Biomembr.*, 2016, **1858**(6), 1244–1253.

17 C. K. Choi, M. Vicente-Manzanares, J. Zareno, L. A. Whitmore, A. Mogilner and A. R. Horwitz, Actin and alpha-actinin orchestrate the assembly and maturation of nascent adhesions in a myosin II motor-independent manner, *Nat. Cell Biol.*, 2008, **10**(9), 1039.

18 S. Teixeira, M. P. Ferraz and F. J. Monteiro, Biocompatibility of highly macroporous ceramic scaffolds: cell adhesion and morphology studies, *J. Mater. Sci.: Mater. Med.*, 2008, **19**(2), 855–859.

19 D. Toomre and D. J. Manstein, Lighting up the cell surface with evanescent wave microscopy, *Trends Cell Biol.*, 2001, **11**(7), 298–303.

20 S. Q. Dai, T. Y. Yu, J. W. Zhang, H. Lu, J. Z. Dou, M. M. Zhang, C. Dong, J. L. Di and J. L. Zhao, Real-time and wide-field mapping of cell-substrate adhesion gap and its evolution *via* surface plasmon resonance holographic microscopy, *Biosens. Bioelectron.*, 2021, **174**, 112826.

21 T. Son, J. Seo, I. H. Choi and D. Kim, Label-free quantification of cell-to-substrate separation by surface plasmon resonance microscopy, *Opt. Commun.*, 2018, **422**, 64–68.

22 B. Liu, S. A. Rotenberg and M. V. Mirkin, Scanning electrochemical microscopy of living cells: Different redox activities of nonmetastatic and metastatic human breast cells, *Proc. Natl. Acad. Sci. U. S. A.*, 2000, **97**(18), 9855–9860.

23 G. Valenti, S. Scarabino, B. Goudeau, A. Lesch, M. Jovic, E. Villani, M. Sentic, S. Rapino, S. Arbault, F. Paolucci and N. Sojic, Single Cell Electrochemiluminescence Imaging:

From the Proof-of-Concept to Disposable Device-Based Analysis, *J. Am. Chem. Soc.*, 2017, **139**(46), 16830–16837.

24 S. Voci, B. Goudeau, G. Valenti, A. Lesch, M. Jovic, S. Rapino, F. Paolucci, S. Arbault and N. Sojic, Surface-Confined Electrochemiluminescence Microscopy of Cell Membranes, *J. Am. Chem. Soc.*, 2018, **140**(44), 14753–14760.

25 Y. Chen, X. Gou, C. Ma, D. Jiang and J.-J. Zhu, A Synergistic Coreactant for Single-Cell Electrochemiluminescence Imaging: Guanine-Rich ssDNA-Loaded High-Index Faceted Gold Nanoflowers, *Anal. Chem.*, 2021, **93**(21), 7682–7689.

26 J. Zhang, R. Jin, D. Jiang and H.-Y. Chen, Electrochemiluminescence-Based Capacitance Microscopy for Label-Free Imaging of Antigens on the Cellular Plasma Membrane, *J. Am. Chem. Soc.*, 2019, **141**(26), 10294–10299.

27 Y. Liu, H. Zhang, B. Li, J. Liu, D. Jiang, B. Liu and N. Sojic, Single Biomolecule Imaging by Electrochemiluminescence, *J. Am. Chem. Soc.*, 2021, **143**(43), 17910–17914.

28 H. Ding, W. Guo and B. Su, Imaging Cell-Matrix Adhesions and Collective Migration of Living Cells by Electrochemiluminescence Microscopy, *Angew. Chem., Int. Ed.*, 2020, **59**(1), 449–456.

29 H. Ding, P. Zhou, W. Fu, L. Ding, W. Guo and B. Su, Spatially Selective Imaging of Cell-Matrix and Cell-Cell Junctions by Electrochemiluminescence, *Angew. Chem., Int. Ed.*, 2021, **60**(21), 11769–11773.

30 J. K. Leland and M. J. Powell, Electrogenerated Chemiluminescence – an Oxidative-Reduction Type Ecl Reaction Sequence Using Tripropyl Amine, *J. Electrochem. Soc.*, 1990, **137**(10), 3127–3131.

31 N. Wang, H. Gao, Y. Li, G. Li, W. Chen, Z. Jin, J. Lei, Q. Wei and H. Ju, Dual Intramolecular Electron Transfer for *In Situ* Coreactant-Embedded Electrochemiluminescence Microimaging of Membrane Protein, *Angew. Chem., Int. Ed.*, 2021, **60**(1), 197–201.

32 J. Yu, H. Saada, R. Abdallah, G. Loget and N. Sojic, Luminescence Amplification at $BiVO_4$ Photoanodes by Photoinduced Electrochemiluminescence, *Angew. Chem., Int. Ed.*, 2020, **59**(35), 15157–15160.

33 Y. R. Zhao, J. Descamps, S. Ababou-Girard, J. F. Bergamini, L. Santinacci, Y. Leger, N. Sojic and G. Loget, Metal-Insulator-Semiconductor Anodes for Ultrastable and Site-Selective Upconversion Photoinduced Electrochemiluminescence, *Angew. Chem., Int. Ed.*, 2022, **61**(20), e202201865.

34 Y. R. Zhao, J. Yu, G. B. Xu, N. O. Sojic and G. R. E. Loget, Photoinduced Electrochemiluminescence at Silicon Electrodes in Water, *J. Am. Chem. Soc.*, 2019, **141**(33), 13013–13016.

35 M. P. Dinel, S. Tartaggia, G. Q. Wallace, D. Boudreau, J. F. Masson and F. Polo, The Fundamentals of Real-Time Surface Plasmon Resonance/Electrogenerated Chemiluminescence, *Angew. Chem., Int. Ed. Engl.*, 2019, **58**(50), 18202–18206.

36 Y. Zhao, L. Bouffier, G. Xu, G. Loget and N. Sojic, Electrochemiluminescence with semiconductor (nano) materials, *Chem. Sci.*, 2022, **13**(9), 2528–2550.

37 J. Mostany, B. R. Scharifker, K. Saavedra and C. Borrás, Electrochemical nucleation and the classical theory: Overpotential and temperature dependence of the nucleation rate, *Russ. J. Electrochem.*, 2008, **44**(6), 652–658.

38 W. L. Wallace and A. J. Bard, Electrogenerated chemiluminescence. 35. Temperature dependence of the ECL efficiency of tris(2,2'-bipyridine)rubidium(2+) in acetonitrile and evidence for very high excited state yields from electron transfer reactions, *J. Phys. Chem.*, 1979, **83**(10), 1350–1357.

39 J. Van Houten and R. J. Watts, Temperature dependence of the photophysical and photochemical properties of the tris(2,2'-bipyridyl)ruthenium(II) ion in aqueous solution, *J. Am. Chem. Soc.*, 1976, **98**(16), 4853–4858.

40 F. Bolletta and S. Bonafede, Chemiluminescence and Electrochemiluminescence of Coordination-Compounds, *Pure Appl. Chem.*, 1986, **58**(9), 1229–1232.

41 J. Woo, J. Kim and J. Kim, Indium tin oxide bipolar electrodes modified with Pt nanoparticles encapsulated inside dendrimers as sensitive electrochemiluminescence platforms, *J. Electroanal. Chem.*, 2022, **906**, 115998.

42 R. Huang, M.-Y. Wei and L.-H. Guo, Enhanced electrogenerated chemiluminescence of/tripropylamine system on indium tin oxide nanoparticle modified transparent electrode, *J. Electroanal. Chem.*, 2011, **656**(1–2), 136–139.

43 Y. Toshimitsu, Y. Katayama and T. Miura, Electrode reactions of ruthenium–bipyridine complex in amide-type ionic liquids, *Electrochim. Acta*, 2012, **82**, 43–47.

44 A. Degli Esposti, V. Fattori, C. Sabatini, G. Casalbore-Miceli and G. Marconi, The electron transfer rate of large TPA based compounds: a joint theoretical and electrochemical approach, *Phys. Chem. Chem. Phys.*, 2005, **7**(21), 3738–3743.

45 C. Ma, Z. Xing, X. Gou, L. P. Jiang and J. J. Zhu, A temperature-tuned electrochemiluminescence layer for reversibly imaging cell topography, *Chem. Sci.*, 2022, **13**(46), 13938–13947.

46 X. Yang, J. H. Lee, S. Kattel, B. Xu and J. G. Chen, Tuning Reaction Pathways of Electrochemical Conversion of CO2 by Growing Pd Shells on Ag Nanocubes, *Nano Lett.*, 2022, **22**(11), 4576–4582.

47 A. V. Lyulin, S. Sengupta, A. Varughese, P. Komarov and A. Venkatnathan, Effect of Annealing on Structure and Diffusion in Hydrated Nafion Membranes, *ACS Appl. Polym. Mater.*, 2020, **2**(11), 5058–5066.

48 S. F. Douman, E. Brennan, E. I. Iwuoha and R. J. Forster, Wireless Electrochemiluminescence at Nafion-Carbon Microparticle Composite Films, *Anal. Chem.*, 2017, **89**(21), 11614–11619.

49 Z. M. Hu, C. J. Seliskar and W. R. Heineman, Voltammetry of [Re(DMPE)(3)](+) at ionomer-entrapped composite-modified electrodes, *Anal. Chem.*, 1998, **70**(24), 5230–5236.

50 Y. Chen, Y. Jiang, Z. Lin, J. Sun, L. Zhang and G. Chen, An electrochemiluminescent detector based on multi-wall-carbon-nanotube/Nafion/Ru(bpy)3(2+) composite film modified heated-electrode, *J. Nanosci. Nanotechnol.*, 2009, **9**(4), 2303–2309.

51 D. Han, B. Goudeau, D. Jiang, D. Fang and N. Sojic, Electrochemiluminescence Microscopy of Cells: Essential Role of Surface Regeneration, *Anal. Chem.*, 2021, **93**(3), 1652–1657.

52 C. Ma, M. X. Wang, H. F. Wei, S. Wu, J. R. Zhang, J. J. Zhu and Z. Chen, Catalytic route electrochemiluminescence microscopy of cell membranes with nitrogen-doped carbon dots as nano-coreactants, *Chem. Commun.*, 2021, **57**(17), 2168–2171.

53 D. N. Han, B. Goudeau, D. Manojlovic, D. C. Jiang, D. J. Fang and N. Sojic, Electrochemiluminescence Loss in Photobleaching, *Angew. Chem., Int. Ed.*, 2021, **60**(14), 7686–7690.